Supporting Information

CO_2 Photoreduction via Quantum Tunneling: Thin-TiO_2-Coated GaP with Coherent Interface to Achieve Electron Tunneling

Li-Fen Li, Ye-Fei Li* and Zhi-Pan Liu*

Collaborative Innovation Center of Chemistry for Energy Material, Key Laboratory of Computational Physical Science (Ministry of Education), Shanghai Key Laboratory of Molecular Catalysis and Innovative Materials, Department of Chemistry, Fudan University, Shanghai 200433, China

Email: yefeil@fudan.edu.cn; zpliu@fudan.edu.cn

Table of Contents

Part I. Calculation Details

S1. Method to Determine the Low-strain Interface

In this work, we use a modified phenomenological theory of Martensitic crystallography (PTMC) to predict the ORs of low-strain interfaces. First, we briefly review the algorithm of original PTMC. In PTMC, which involves follows three steps:

i. Determine the Deformation Gradient F Matrix

Let us define the lattice parameters of two crystals as T and M, both (3x3) matrices. A deformation gradient F matrix transforms an initial lattice T to a final lattice M, as defined by formula (1).

$$\mathbf{FT} = \mathbf{M} \qquad (1)$$

ii. Construct Cauchy–Green Deformation Tensor

The deformation gradient F can be decomposed to a pure rotation (**R**) and a pure stretch (**U**). We remove the pure rotation in F by constructing the Cauchy-Green deformation tensor, as shown in formula (2) and (3).

$$\mathbf{F} = \mathbf{RU} \qquad (2)$$

$$C = F^TF = U^TR^TRU = U^TU \qquad (3)$$

iii. Find the Strain Invariant Lines and Strain Invariant Plane

Next, we perform the eigendecomposition of Cauchy-Green deformation tensor:

$$\mathbf{Ce_i} = I_i\mathbf{e_i} \quad (i=1,2,3) \qquad (4)$$

The calculated eigenvalues (I_i) and eigenvectors ($\mathbf{e_i}$) represent the principal stretches and corresponding directions. To distinguish the principal stretches, we set $I_1<I_2<I_3$ for convenience. For Martensitic transformation, the principal stretches should be

$$I_1 <1,\ I_2\approx 1,\ I_3 >1 \qquad (5)$$

$\mathbf{e_2}$ is the direction of strain invariant line (***sil***). Another strain invariant line can be determined by the linear combination of eigenvectors $\mathbf{e_1}$ and $\mathbf{e_3}$ by following equations:

$$a^2 + c^2 = 1 \qquad (6)$$

$$a^2I_1 + c^2I_3 = 1 \qquad (7)$$

$$\boldsymbol{sil_2} = a\mathbf{e_1} + c\mathbf{e_3} \qquad (8)$$

The normal to the strain invariant plane (***sip***) is given by

$$\boldsymbol{sip} = e_2 \times \boldsymbol{sil_2} \qquad (9)$$

The strain invariant plane provides information of orientation relations (ORs) for low-strain interfaces between two crystals.

From the above procedure, we can find that the lattice parameters of the two crystals are the only inputs in PTMC. For a specified crystal, we can take infinite unit cells, with different sizes and shapes. For instance, in a 2-D cubic lattice, as shown in Figure S1, the shapes of the unit cell can be square or parallelogram, while the size can be the primitive cell or supercell. By changing the definition of unit cells, we can obtain various lattice parameters for a given crystal. Utilizing the set of lattice parameters as PTMC inputs, we can screen out the low-strain interfaces between two crystals.

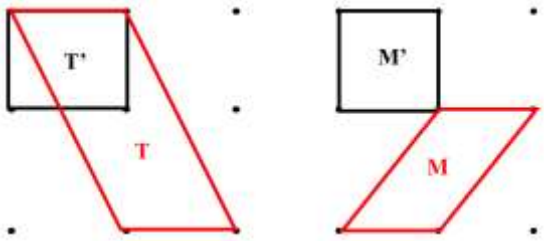

Figure S1. An example of different supercell for 2D cubic crystal.

Mathematically, the varieties of lattice parameters can be represented by the lattice parameter of a primitive cell multiplied by a transformation matrix. Let us define two primitive cells **T'** and **M'** describe two crystal structures compose a heterojunction. Then other unit cells are given by

$$T = AT' \qquad (10)$$

$$M = BM' \qquad (11)$$

T and **M** denote the unit cells with different sizes and shapes, and **A** and **B** the transformation matrices. In the transformation matrix, all elements should be integer due to the translational symmetry. The shape change of unit cell is defined by non-diagonal elements, while the volume change is determined by the determinant. By sampling the transformation matrices **A** and **B**, we can sample the lattice correspondence between two crystals and then derive all possible strain invariant planes.

To construct the transformation matrices **A** and **B**, we use the following strategy: (i) Fix the diagonal elements of **A** and **B** to be {1, 1, 1}; (ii) Exhaust the non-diagonal elements within {-2, -1, 0, 1, 2}; (iii) Permutate the row vectors of **A** to exchange the lattice vectors; (iv) eliminate the nonphysical matrices **A** and **B** with negative determinant.

With the lattice correspondences, we then use PTMC to determine the ORs of low-strain interfaces. According to PTMC, the existence of strain invariant plane requires one principle stretch equals 1.[1-3] Thus, the lattice correspondences where I_2 deviate from 1 is rejected. In this work, the tolerance of I_2 is set to be 0.9~1.1. From the OR, we then can construct the interface structure and perform stochastic surface walking (SSW) global structural search to ensure we find the stable interface. The overall flowchart is shown in Figure S2.

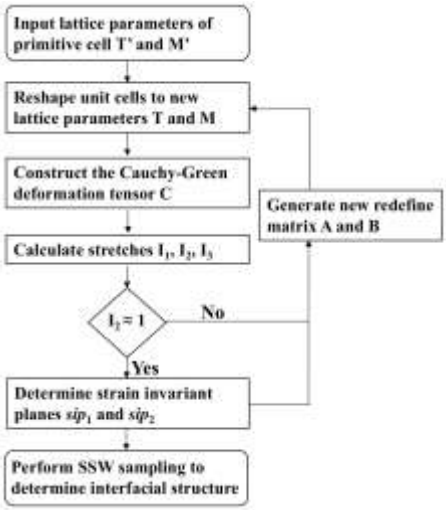

Figure S2. Flowchart of determining the interfacial structure of heterojunction.

S2. Optimization Strategy for GaP/TiO_2 Interfaces

It is no doubt that the interface atoms must relax the strain by expanding/contracting the lattice to accommodate two phases. This is as shown in Figure S3. The in-plane lattice of coating must relax to its bulk lattice with the increase of coating layer. Even for the thin coating, the lattice of the coating layer may also not follow the lattice of the substrate. For example, previous experiments on $Ba_{1-x}Sr_xTiO_3/BaTiO_3/SrTiO_3$have shown that the lattice of coherent coating can be determined by the lattice of coating material rather than the substrate.[4] Because of the supercell approach utilized in the current plane-wave DFT method, the lattice in modelling the interface needs to take caution.

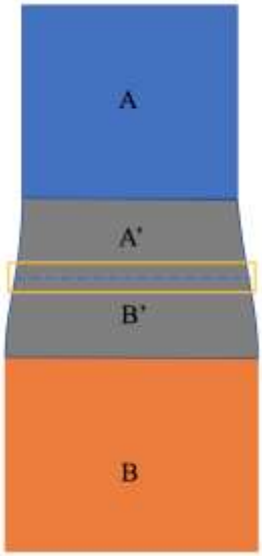

Figure **S3**. Schematic drawing for the solid-solid interface. A and B denote the phase of coating and substrate, respectively. The gray region represents the compliant layer, and the blue dotted line is the interface. The lattices of both A' and B' phase in the compliant layer need to expand or contract to reduce the strain.

In this work, we focus on the coherent interface, which has a low lattice match. Our best interface model for GaP/TiO_2 ((001)TiO_2//(100)GaP) identified has a very small lattice mismatch, only 2%. This suggests that few thin layers of atoms at the interface can accommodate the mismatch. To model the interface in supercell approach, we typically utilize a GaP substrate with 8 layers (2.16 nm). By growing TiO_2 layers on GaP gradually, we found that if the lattice is relaxed, we can find that the TiO_2 layers up to 4 nm thickness provides the correct trend for the interface energy, which is expected from the common knowledge. However, if the lattice is fixed at GaP lattice, the more TiO_2 layers are present, the higher the interface energy will be (apparently due to the unphysical lattice for TiO_2 bulk). We therefore select the in-plane relaxed model for our interface. It should be mentioned that due to the low lattice mismatch, when the TiO_2 is below 1nm thick, the electronic structure, in particular the band alignment and optical absorption, are essentially the same with or without the lattice relaxation.

S3. SSW global structural search

The SSW algorithm[5-6] features an automated climbing mechanism to manipulate one minimum to a high energy configuration along one random direction, which is inherited from the bias potential driven constrained-Broyden-dimer (BP-CBD) method for TS location developed in the group.[7] The method has been successfully utilized for predicting the structure of finite clusters with complex PES, such as C100 fullerene. [5-6] In one particular SSW step, labeled as *i*, a modified PES $V_{m\text{-}to\text{-}H}$, as shown in eqn (12), is utilized for moving from the current minimum, $\mathbf{R}_i^m$ to a high energy configuration $\mathbf{R}_i^H$, in which a series of bias Gaussian potential v_n (*n* is the index of the bias potential, $n = 1,2...H$) is added one by one consecutively along the direction $\boldsymbol{N}_i^n$.

$$V_{m-to-H} = V_{real} + \sum_{n=1}^{H} v_n$$

$$= V_{real} + \sum_{n=1}^{H} w_n \cdot exp\left[-\left((\boldsymbol{R}^t - \boldsymbol{R}_t^{n-1}) \cdot \boldsymbol{N}_i^n\right)^2/(2 \times ds^2)\right] \quad (12)$$

$$\boldsymbol{F}_{tot} = \boldsymbol{F}_{real} + \sum_n w_n \cdot exp\left[-\frac{\left((\boldsymbol{R}^t - \boldsymbol{R}_t^{n-1}) \cdot \boldsymbol{N}_i^n\right)^2}{2 \times ds^2}\right] \cdot \frac{(\boldsymbol{R}^t - \boldsymbol{R}_t^{n-1}) \cdot \boldsymbol{N}_i^n}{ds^2} \cdot \boldsymbol{N}_i^n \quad (13)$$

where **R** is the coordination vector of the structure and V_{real} represents the unmodified PES; R_t^n are the n^{th} local minima along the movement trajectory on the modified PES which is created after adding *n* Gaussian functions (see Fig. 1a). The PES at $\mathbf{R}_t^n$ is thus defined by $V_{m\text{-}to\text{-}n} = V_{\text{real}} + \sum_{k=1}^{n} v_k$. The Gaussian function is controlled by its height w and its width ds, and is always added along one particular walking direction as defined by $\boldsymbol{N}^n$. Once the R_i^H is reached, all bias potentials are removed, and the local optimization is performed to quench the structure to a new minimum.

S4. Transmission Coefficients for Electron Tunneling through Incoherent Interface

In practice, incoherent interfaces are more common than coherent interfaces in heterojunctions, since atomic mismatch can easily occur during synthesis. Therefore, it is important to establish the influence of incoherent interface to the electron tunneling. To this end, we construct an incoherent interface, which has a larger strain (10%) from our modified PTMC method as shown in Figure S2. The interface follows the OR of $(101)_{TiO_2}//(111)_{GaP}$; $[010]_{TiO_2}//[110]_{GaP}$ (denoted as OR_4). The structure and the wavefunctions for VBM and CBM are shown in the Figure S4. The results show that both VBM and

CBM are localized at a few atoms at the interface. The localized states would act as trapping states and generally increase the effective masses of carriers. For instance, along with the Γ-X direction, the effective mass of electron in OR_4 is 0.62 m_e, larger than that in heterojunction OR1 (0.16 m_e). Then, we increase m_e* at the interface to 0.62 m_e and recalculate the transmission coefficients of 1 nm TiO_2 coating. The results are shown in Figure 4b (the dashed line), which is much lower compared to that of the coherent interface.

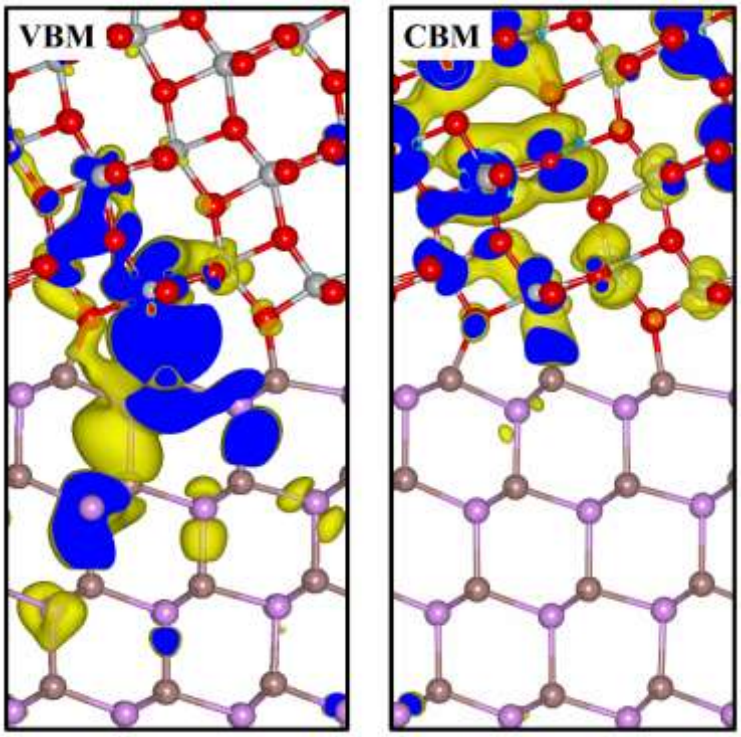

Figure S4. Isosurfaces for wavefunctions of VBM and CBM in an incoherent interface. Gray balls: Ti; Red balls: O; Brown balls: Ga; Purple balls: P.

Part II. Tables and Figures for Supplements

S1. ORs and Lattice parameters for GaP/TiO_2 interfaces

Table S1. Orientation relations (OR) and surface lattice parameters for GaP/TiO_2 heterojunctions with with reasonable strain (<10%). The *a* and *b* are the length of surface vectors, while θ is the angle between two surface vectors.

	$OR_{TiO_2//GaP}$	TiO_2			GaP			strain
		a/Å	*b*/Å	θ/°	*a*/Å	*b*/Å	θ/°	
1	(100)//(113)	3.78	18.97	90	3.85	19.27	84.26	1.85%
2	(112)//(100)	5.44	5.34	90	5.45	5.45	90	2.06%
3	(001)//(100)	3.78	3.78	90	3.86	3.86	90	2.12%
4	(110)//(110)	5.44	18.62	91.25	5.45	19.27	90	3.49%
5	(112)//(110)	5.34	10.89	90	5.45	11.56	90	6.15%
6	(101)//(101)	3.78	10.21	90	3.85	10.9	90	6.76%
7	(110)//(310)	5.44	9.31	88.75	5.45	8.62	90	8.00%

S2. ORs and Lattice parameters for interfaces of AlSb/TiO_2, ZnTe/TiO_2, and $MAPbI_3$/TiO_2 hetero-materials

Table S2. OR and surface lattice parameters for AlSb/TiO_2, ZnTe/TiO_2, and $MAPbI_3$/TiO_2 hetero-materials with reasonable strain (<10%). The *a* and *b* are the length of surface vectors, while θ is the angle between two surface vectors.

	OR	*a*/Å	*b*/Å	θ/°	*a*/Å	*b*/Å	θ/°	strain
			AlSb			TiO_2		
1	(110)//(101)	7.51	10.63	90	7.55	10.21	90	4%
2	(111)//(112)	7.51	11.48	71	7.63	11.99	73	4%
3	(113)//(111)	9.70	16.80	73	10.21	16.02	75	5%
			ZnTe			TiO_2		
1	(111)//(101)	7.47	11.41	71	7.55	10.89	70	5%
2	(111)//(112)	7.47	11.41	71	7.63	11.99	73	5%
3	(113)//(111)	9.65	16.71	73	10.21	16.02	75	6%
			$MAPbI_3$			TiO_2		
1	(010)//(110)	8.84	8.91	60	9.31	9.31	61	5%
2	(001)//(001)	8.84	8.84	90	8.44	8.44	90	5%
3	(001)//(112)	12.50	12.69	90	11.99	12.13	89	5%

S3. The density of states for GaP/TiO_2 hetero-materials

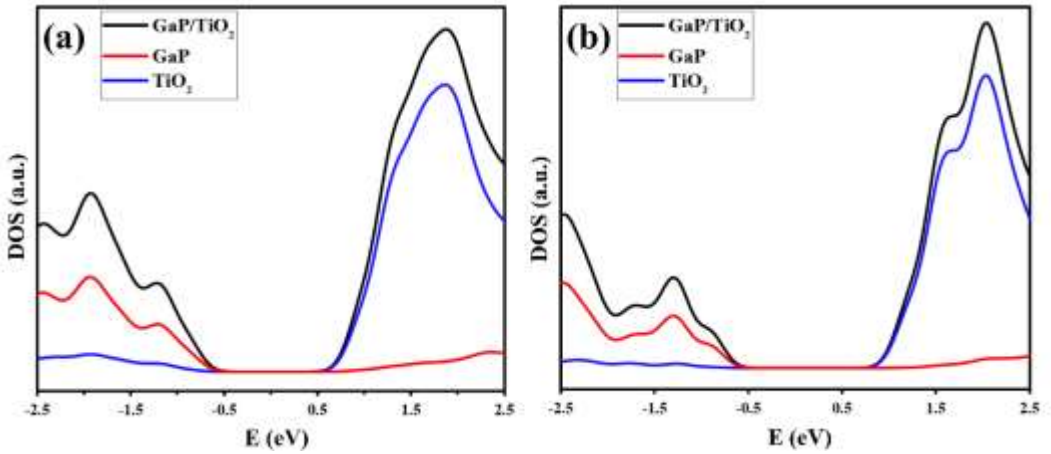

Figure S5. Density of states for GaP/TiO_2 hetero-materials. (a) OR_2 ($(101)_{TiO_2}//(110)_{GaP}$) and (b) OR_3 ($(112)_{TiO_2}//(100)_{GaP}$). The black line is the total density of states, while the blue and red lines are the projected density of states for TiO_2 and GaP, respectively. The energy of *E*-axis refers to the Fermi level as zero.

S4. Isosurfaces for wavefunctions of VBM and CBM in GaP/TiO_2 hetero-materials for OR_2 and OR_3

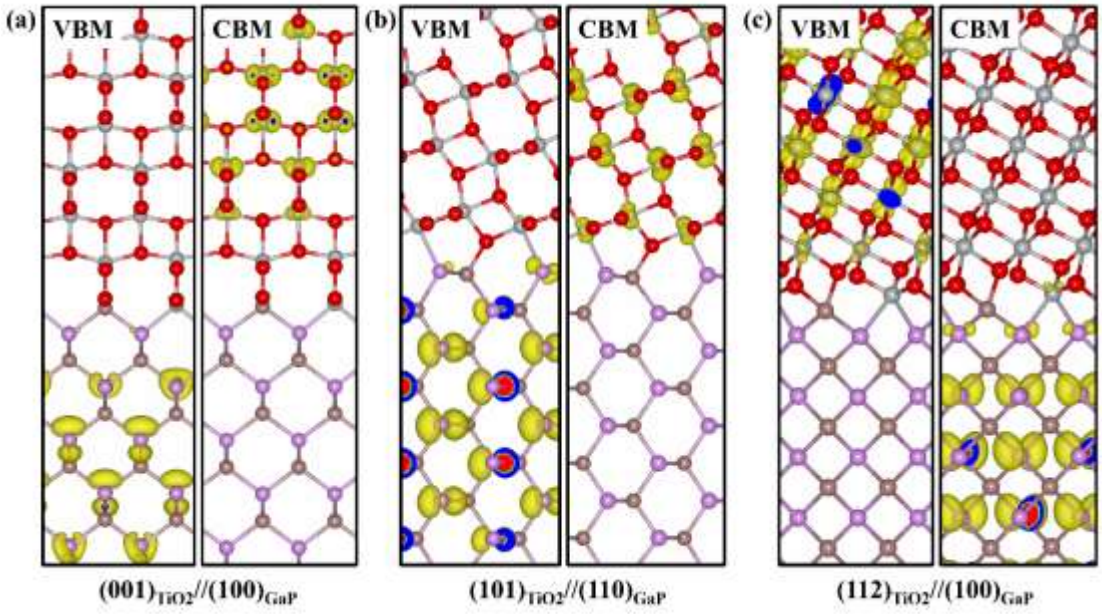

Figure S6 Isosurfaces for wavefunctions of VBM and CBM in bulk GaP/TiO_2 hetero-materials with (a) OR_1, (b) OR_2 and (c) OR_3. The cutoff is chosen as 0.02 $|e|/Å^3$. Gray balls: Ti; Red balls: O; Brown balls: Ga; Purple balls: P.

S5. Electronic structures for GaP/TiO2 hetero-material by PBE functional

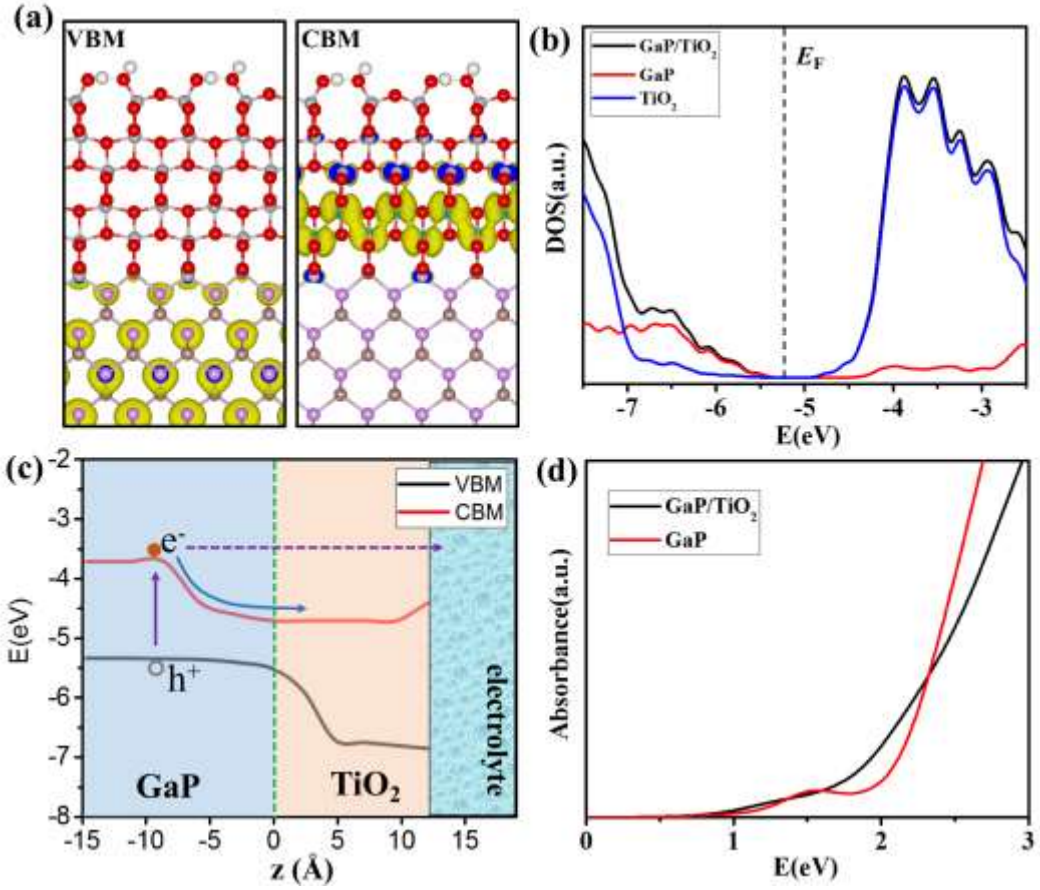

Figure S7 Electronic structures for GaP/TiO_2 hetero-material with $(001)_{TiO2}//(100)_{GaP}$. All the calculations are based on PBE functional (a) Isosurfaces of wavefunctions for valence band maximum (VBM) and conduction band minimum (CBM) in GaP/TiO_2 hetero-material. The value of isosurfaces is 0.02 |e|/Å^3. Gray balls: Ti; Red balls: O; Brown balls: Ga; Purple balls: P. (b) The density of states (DOS) for the GaP/TiO_2 hetero-material. The black line is the total density of states, while the blue and red lines are the projected density of states for TiO_2 and GaP compositions, respectively. The energy of *E*-axis is relative to the vacuum level as zero. The dotted line is the position of the Fermi level. (c) The band diagram of $(001)_{TiO2}//(100)_{GaP}$ hetero-material. The z-axis represents the position relative to the GaP/TiO_2 interface. The red line is the band diagram of CBM, while the black line is the band diagram of VBM. (d) Optical absorption for pure GaP (red line) and GaP/TiO_2 hetero-material (black line).

S6. The spatial distribution of spin density for TS1 of CO_2 reduction

Figure S8 Spatial distribution of spin density for TS1 of CRR on anatase (001). Gray balls: Ti; Red balls:

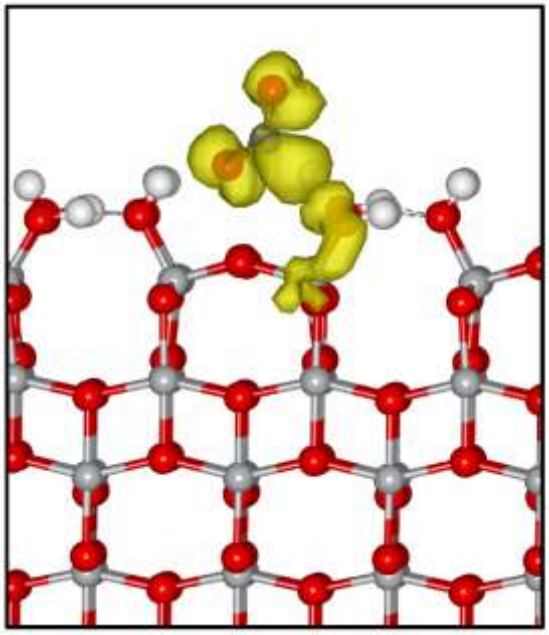

O; White ball: H.

S7. The band alignment of 21 inorganic semiconductors and seven inorganic-organic hybrid halide perovskites

We have screened out the suitable CO_2 reduction candidates from a set of semiconductors involving twenty-one inorganic semiconductors (BN, C, Si, Ge, AlP, AlAs, AlSb, GaP, GaAs, GaSb, InP, InAs, InSb, ZnSe, ZnTe, CdS, CdTe, ZnO, and GaN) and seven organic-inorganic hybrid halide perovskites ($MASn_{0.5}Pb_{0.5}I_3$, $MASn_3I_3$, $MAPbI_2Br$, $MAPbBr_3$, $FAPbI_3$, $MAPbI_3$). From their band levels, only three inorganic materials out of 21 candidates have suitable band positions, as shown in Figure S8, namely AlSb, ZnTe, and AlAs, which can absorb visible light and provide reactive electrons for CO_2 reduction. On the other hand, all seven hybrid halide perovskites solar cells have appropriate band positions for CO_2 reduction.

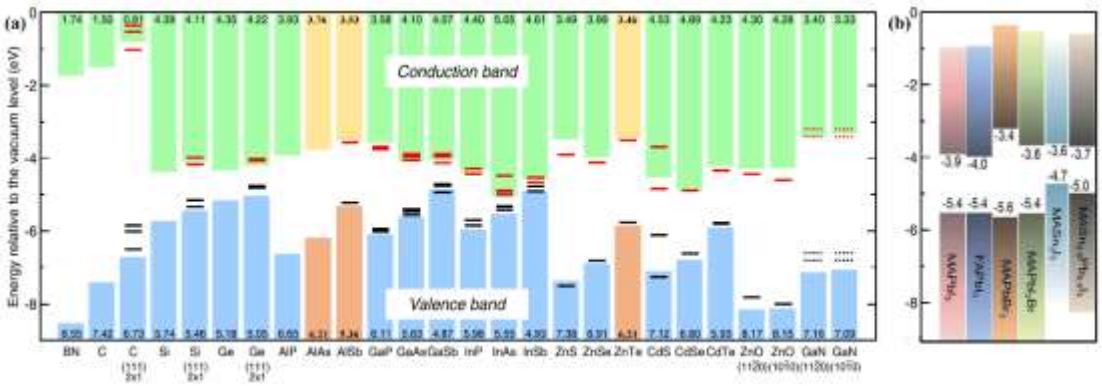

Figure S9 Band alignment of twenty-one fundamental semiconductors and seven hybrid halide perovskites ($MASn_{0.5}Pb_{0.5}I_3$, $MASn_3I_3$, $MAPbI_2Br$, $MAPbBr_3$, $FAPbI_3$, $MAPbI_3$) from available

experimental data and theoretical calculations in previous literature.[8-11] Figure (a) is reproduced with permission from Reference 9.

S8. The spatial distribution of spin density and isosurfaces for wavefunctions of photo hole and electron in GaP/TiO_2 hetero-materials for singlet-triplet excitation.

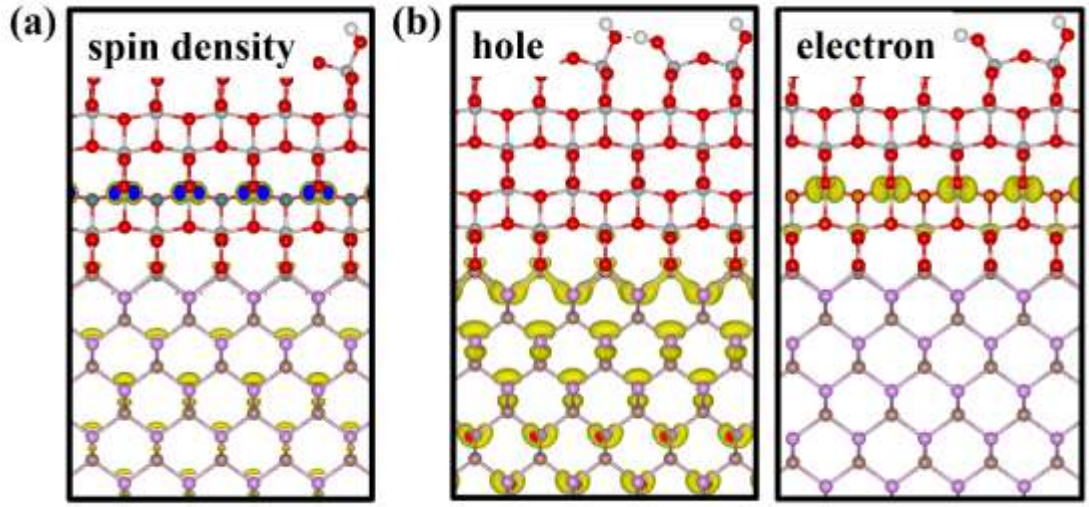

Figure S10 (a) The spatial distribution of spin density and (b) isosurfaces for wavefunctions of photo hole and electron in GaP/TiO_2 hetero-materials for singlet-triplet excitation.

S9. Phase diagrams of *H on the GaP/TiO_2 heterojunction

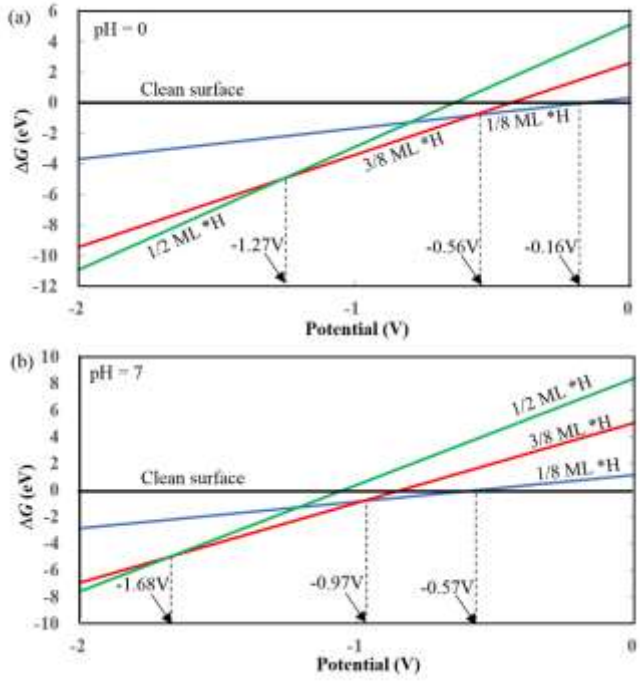

Figure S11. Phase diagrams of *H on the GaP/TiO_2 heterojunction: (a) pH = 0, (b) pH = 7.

REFERENCES

(1). Bowles, J.; Mackenzie, J. The Crystallography of Martensite Transformations I. *Acta metall.* **1954,** *2*, 129-137.

(2). Mackenzie, J.; Bowles, J. The Crystallography of Martensite Transformations II. *Acta metall.* **1954,** *2*, 138-147.

(3). Wayman, C. The Phenomenological Theory of Martensite Crystallography: Interrelationships. *Metall. Mater. Trans. A* **1994,** *25*, 1787-1795.

(4). Terai, K.; Lippmaa, M.; Ahmet, P.; Chikyow, T.; Fujii, T.; Koinuma, H.; Kawasaki, M. In-plane Lattice Constant Tuning of an Oxide Substrate with $Ba_{1-x}Sr_xTiO_3$ and $BaTiO_3$ Buffer Layers. *Appl. Phys. Lett.* **2002,** *80*, 4437-4439.

(5). Shang, C.; Liu, Z.-P. Stochastic Surface Walking Method for Structure Prediction and Pathway Searching. *J. Chem. Theory Comput.* **2013,** *9*, 1838-1845.

(6). Zhang, X.-J.; Shang, C.; Liu, Z.-P. From Atoms to Fullerene: Stochastic Surface Walking Solution for Automated Structure Prediction of Complex Material. *J. Chem. Theory Comput.* **2013,** *9*, 3252-3260.

(7). Shang, C.; Liu, Z.-P. Constrained Broyden Dimer Method with Bias Potential for Exploring Potential Energy Surface of Multistep Reaction Process. *J. Chem. Theory Comput.* **2012,** *8*, 2215-2222.

(8). Gruneis, A.; Kresse, G.; Hinuma, Y.; Oba, F. Ionization Potentials of Solids: The Importance of Vertex Corrections. *Phys. Rev. Lett.* **2014,** *112*, 5.

(9). Hinuma, Y.; Gruneis, A.; Kresse, G.; Oba, F. Band Alignment of Semiconductors from Density-functional Theory and Many-body Perturbation Theory. *Phys. Rev. B* **2014,** *90*, 16.

(10). Chueh, C. C.; Li, C. Z.; Jen, A. K. Y. Recent Progress and Perspective in Solution-processed Interfacial Materials for Efficient and Stable Polymer and Organometal Perovskite Solar Cells. *Energ. Environ. Sci.* **2015,** *8*, 1160-1189.

(11). Zardetto, V.; Williams, B. L.; Perrotta, A.; Di Giacomo, F.; Verheijen, M. A.; Andriessen, R.; Kessels, W. M. M.; Creatore, M. Atomic Layer Deposition for Perovskite Solar Cells: Research Status, Opportunities and Challenges. *Sustain. Energ. Fuels* **2017,** *1*, 30-55.